

Label-free identification of human coronary atherosclerotic plaque based on a three-dimensional quantitative assessment of multiphoton microscopy images

RONGLI ZHANG,^{1,2,3,4}  ZHONGBIAO XU,⁵ JUNHAI HAO,⁶ JIA YU,^{3,4} ZHIYI LIU,⁷ SHUN LIU,^{3,4,8} WANWEN CHEN,² JIAHUI ZHOU,² HUI LI,^{3,4,9} ZHANYI LIN,^{1,2,10} AND WEI ZHENG^{3,4,11}

¹Guangdong Provincial Geriatrics Institute, Guangdong Provincial People's Hospital, Guangdong Academy of Medical Sciences, Guangzhou, Guangdong 510080, China

²Department of Cardiology, Guangdong Provincial Cardiovascular Institute, Guangdong Provincial People's Hospital, Guangdong Academy of Medical Sciences, Guangzhou, Guangdong 510080, China

³Research Center for Biomedical Optics and Molecular Imaging, Shenzhen Key Laboratory for Molecular Imaging, Guangdong Provincial Key Laboratory of Biomedical Optical Imaging Technology, Shenzhen Institute of Advanced Technology, Chinese Academy of Sciences, Shenzhen 518055, China

⁴CAS Key Laboratory of Health Informatics, Shenzhen Institute of Advanced Technology, Chinese Academy of Sciences, Shenzhen 518055, China

⁵Department of Radiotherapy, Cancer Center, Guangdong Provincial People's Hospital, Guangdong Academy of Medical Sciences, Guangzhou, Guangdong 510080, China

⁶Department of Intensive Care Unit of Cardiovascular Surgery, Guangdong Cardiovascular Institute, Guangdong Provincial People's Hospital, Guangdong Academy of Medical Sciences, Guangzhou, Guangdong 510080, China

⁷State Key Laboratory of Modern Optical Instrumentation, College of Optical Science and Engineering, International Research Center for Advanced Photonics, Zhejiang University, Hangzhou, Zhejiang 310058, China

⁸School of Optoelectronic Engineering, Xi'an Technological University, Xi'an 710021, China

⁹hui.li@siat.ac.cn

¹⁰linzhanyi@hotmail.com

¹¹zhengwei@siat.ac.cn

Abstract: The rupture of coronary atherosclerotic plaque (CAP) and the resulting intracoronary thrombosis account for most acute coronary syndromes. Thus, the early identification and risk assessment of CAP is crucial for timely medical intervention. In this study, we propose a quantitative and label-free method for human CAP identification using multiphoton microscopy (MPM) and three-dimensional (3D) image analysis techniques. By detecting the intrinsic MPM signals, the microstructures of collagen and elastin fibers within normal and CAP-lesioned human coronary artery walls were imaged. Using a 3D gray level co-occurrence matrix method and 3D weighted vector summation algorithm, quantitative indicators that characterize the spatial texture and orientation features of the fibers were extracted. We demonstrate that these indicators show superior accuracy and repeatability over 2D texture features in CAP discrimination. Furthermore, by combining the 3D microstructural indicators, a support vector machine model that classifies CAP from the normal arterial wall with an accuracy of >97% was established. In conjunction with advances in multiphoton endoscopy, the proposed method shows great potential in providing a quantitative, label-free, and real-time tool for the early identification and risk assessment of CAP in the future.

© 2021 Optical Society of America under the terms of the [OSA Open Access Publishing Agreement](#)

1. Introduction

Coronary atherosclerotic plaque (CAP), which is formed from an accumulation of lipids inside the artery wall together with an infiltration of monocytes and other immune cells, has attracted significant attention in clinical and biomedical research for decades [1]. CAP rupture and the resulting intracoronary thrombosis account for most acute coronary syndromes, including unstable angina, myocardial infarctions, and many cases of sudden cardiac death. Thus, they have long been considered a major cause of overall morbidity and mortality worldwide [2,3]. Early identification and risk assessment of CAP are crucial for taking timely intervention measures to reduce the incidence and mortality of acute coronary diseases.

Conventional clinical imaging techniques, such as computed tomography, magnetic resonance imaging, and intravascular ultrasound, are widely used for detecting CAP-related lesions [4–7]. However, they cannot provide adequate sensitivity for early stage identification of CAP due to limited spatial resolution [8,9]. Previous studies have shown that micron-level alterations in the structure and texture of collagen and elastin fibers accompany the development of atherosclerotic plaques within the inner arterial wall [10–12]. Therefore, histological characterization of these fibers may provide effective indicators for the early identification and risk assessment of CAP. Specific staining techniques, such as Masson's trichrome (for collagen) and Verhoeff-Van Gieson (VVG, for elastin), are widely used for histological inspection of collagen and elastin fibers [13,14]. However, the method is limited to *ex vivo* assessment and two-dimensional morphology characterization and involves complicated and time-consuming tissue processing procedures [15]. An intravital, high-resolution, and three-dimensional (3D) imaging method is of considerable interest for the histological characterization of collagen and elastin fibers.

Multiphoton microscopy (MPM) based on two-photon excitation fluorescence (TPEF) and second harmonic generation (SHG) shows great promise for meeting this demand. This technology captures the microstructure of collagen and elastin fibers with a similar level of detail as standard histological inspection by detecting endogenous SHG and TPEF signals, respectively [16]. Moreover, it possesses intrinsic optical sectioning ability, superior tissue penetration depth, and reduced photobleaching and photodamage, which are significant for 3D intravital applications [15,17]. Owing to these attractive advantages, MPM has been applied to the investigation of atherosclerotic lesions [13]. However, the majority of these efforts have been focused on qualitative fiber characterization. As qualitative assessment relies primarily on the researchers' experience, there will be an inevitable degree of variability in image interpretation, which might lead to misjudgment in diagnosis [18]. Hence, a quantitative MPM-compatible evaluation method is desired.

Recent publications show that quantitative fiber features derived from MPM images using two-dimensional (2D) texture analysis techniques, such as fast Fourier transform and gray level co-occurrence matrix (GLCM), may provide potential indicators for atherosclerotic plaque diagnosis [19–21]. However, 2D analyses miss out on microstructural information across different depth planes. Thus, their results heavily rely on a subjective selection of imaging area and depth when volume data are available. This would significantly degenerate the accuracy and repeatability of CAP identification using 2D analysis. Fortunately, 3D image analysis algorithms have emerged in clinical research [22], facilitating a comprehensive microstructural quantification of coronary-artery fibers. Among these algorithms, the 3D GLCM (which is extended from the traditional 2D GLCM) is recognized as the most representative algorithm for spatial texture characterization [23–26], and thus shows potential in providing indispensable indicators for CAP identification. Different from the 3D GLCM that extracts the overall texture feature of volume data, another 3D image analysis technology named 3D weighted vector summation algorithm [27] is capable of quantifying the orientation of fiber-like structures at the voxel level. The algorithm has been demonstrated to be capable of characterizing collagen fibers, neuronal axons, and fibroblasts in the biomedical context of cancer, traumatic brain injury, and engineered breast

tissue [28–30]. Hence, it might be another promising method for CAP identification. Despite the recognized potential of MPM-based 3D microstructural analysis for discerning CAP, its viability has not been extensively evaluated in clinical settings to date.

In this study, we propose to identify CAP on the strength of the quantitative spatial microstructural features of arterial fibers obtained by combining MPM and 3D image analysis algorithms. SHG images of collagen fibers and TPEF images dominated by elastin fibers were simultaneously obtained from human coronary artery specimens. 3D quantitative indicators that characterize the spatial intensity heterogeneity, symmetry, structural isotropy, and directional alignment of the fibers were extracted to distinguish between CAP and normal tissue. Our results demonstrate that these 3D indicators offer unique advantages over 2D microstructural features in CAP identification. Furthermore, a support vector machine (SVM) model uniting the 3D indicators was established to automatically discriminate between normal tissue and CAP lesions. Along with advances in multiphoton endoscopy, the proposed method can potentially result in minimally invasive, label-free, quantitative, and real-time identification and risk assessment of CAP during its early development stage.

2. Materials and methods

2.1. Collection and preparation of human coronary artery specimens

Human coronary artery specimens used in this study were collected from nine heart transplant patients (seven men and two women with a mean age of 47.56 ± 10.73 years old, one specimen each patient) at Guangdong Provincial People's Hospital (Guangzhou, China). After surgical removal, the artery specimens were stored in paraformaldehyde (PFA, 4% [wt./vol.] in phosphate buffered saline [PBS]) and subjected to en face inner-wall MPM imaging, histological inspection, and cross-sectional large-field-of-view (FOV) MPM imaging.

For en face MPM imaging, the artery specimen was first fully opened, and then sandwiched between a custom-designed groove filled with PBS and a glass coverslip, for observation with the objective lens facing the inner arterial wall. MPM images were acquired from several sites per specimen, and a total of 19 normal and 24 CAP regions were imaged.

After imaging, paraffin slices of the specimens were prepared for histological inspection. Hematoxylin and eosin (H&E), Masson, and VVG staining were performed on consecutive slices. H&E staining was used for histopathological diagnosis to determine whether a specific tissue region was normal or a CAP lesion, according to the American Heart Association classification [31]. Masson and VVG staining were used to specifically reveal collagen and elastin organizations, respectively. The obtained fiber organizations were used as the gold standard to evaluate the MPM imaging results.

Finally, the remaining unstained paraffin blocks were used for cross-sectional large-FOV MPM imaging. Using paraffin blocks not only facilitates the preparation and holding of the artery cross section, but it also prevents tissue deformation during imaging, as the human coronary artery wall is only 1–2 mm thick.

All the experimental procedures were approved by the Ethics Committee for Human Research, Guangdong Provincial People's Hospital (Ethics Approval No. GDREC2018225H (R1)), and informed consent from the patients was obtained.

2.2. Cross-sectional large-FOV MPM imaging on the entire artery wall

To capture the MPM image of an intact CAP and the surrounding context for direct comparison, an upright MPM imaging system (A1R-MP, Nikon) was used for large-FOV imaging of the artery cross section. The system was equipped with a Ti: sapphire laser (MaiTai eHP DeepSee, Spectra Physics) and a 25 \times , 1.1 NA water-immersion objective (N25X-APO-MP, Nikon). Using the system, SHG signals from collagen (382.5–407.5 nm) and TPEF signals primarily from elastin

(425–495 nm) in the artery wall were collected at 790 nm excitation, and 3D large-FOV images of $2.45 \text{ mm} \times 1.48 \text{ mm} \times 48 \text{ }\mu\text{m}$ were recorded at $0.5 \times 0.5 \times 4 \text{ }\mu\text{m}^3/\text{voxel}$ dimension. For visualization, the ImageJ (National Institutes of Health) plugin “Stack Focuser” [32] was first used to perform focus stacking on each single-FOV 3D image stack that constitutes the large image. Then, the PreMosa [33] was further used to correct the uneven illumination artifacts and stitch the images automatically.

2.3. En face single-FOV MPM imaging on the inner arterial wall

To obtain angioscopy-view MPM images of the normal and CAP-lesioned tissue, a custom-made spectrum-resolved MPM imaging system was used for en face imaging of the inner arterial wall. A detailed description of the system can be found in our previous papers [34,35]. A femtosecond Ti: sapphire laser (Chameleon Ultra, Coherent) was used as the excitation source. The laser beam was first expanded and then raster scanned by a pair of galvanometer mirrors (TSH8310, Sunny Technology) to create 2D images. After the scanners, the beam passed through a scan lens, a tube lens, and a dichroic mirror (FF685-Di02, Semrock). Then, it was focused on the sample using a water-immersion objective lens (XLUMPLFLN, 20 \times , NA 1.0, Olympus) to excite MPM signals. The excited signals were collected in the epi-direction by the same objective and split from the path of the excitation laser by the dichroic mirror mentioned above. A 680 nm short-pass filter (FF01-680/SP-25, Semrock) was used to remove the residual excitation light, and then the signals were conducted to a spectrograph through a fiber bundle. A linear-array photomultiplier tube (PMT, PMT-16-C, Becker & Hickl GmbH) was utilized to record the signals output from the spectrograph into 16 consecutive spectral channels. Each spectral channel covers a 12.5 nm bandwidth, and the detectable wavelength is tunable from 345 nm to 595 nm. For 3D imaging, a motorized actuator (KMTS25E/M, Thorlabs) was used to translate the objective axially.

En face inner-wall imaging was performed by recording spectrum-resolved 3D image stacks of $300 \times 300 \times 90 \text{ }\mu\text{m}^3$ at 810 nm excitation and $1.2 \times 1.2 \times 3 \text{ }\mu\text{m}^3/\text{voxel}$ dimension. Based on the 3D image stacks, SHG signals from collagen (395–420 nm) and TPEF signals primarily from elastin (432.5–595 nm) were separated according to the emission spectra for subsequent analyses.

2.4. Spatial texture analysis based on 2D and 3D GLCM

To quantify the spatial texture features of collagen and elastin fibers within CAP and the normal inner arterial wall, a 3D GLCM algorithm was used. For a 3D image with g gray levels, the GLCM is an estimate of the second-order joint probability $p(i, j | \vec{d}, g)$ of any two voxels with gray level i and j , which are apart from each other with a displacement vector \vec{d} . Specifically, $\vec{d} = (d_x, d_y, d_z)$, where d_x, d_y and d_z are the distances between these two voxels along the x, y , and z axes, respectively. As shown in Fig. 1(A), \vec{d} determines the relative positions of the pair of voxels, involving distance $|\vec{d}|$ and direction specified by two angles, azimuth α and zenith β [36,37]. From $p(i, j | \vec{d}, g)$, three texture features,

$$\text{Entropy} = - \sum_{i=0}^{g-1} \sum_{j=0}^{g-1} p(i, j) \log(p(i, j)), \quad (1)$$

$$\text{Cluster Shade} = \sum_{i=0}^{g-1} \sum_{j=0}^{g-1} (i + j - \mu_i - \mu_j)^3 p(i, j), \quad (2)$$

and

$$\text{Homogeneity} = \sum_{i=0}^{g-1} \sum_{j=0}^{g-1} \frac{1}{1 + (i - j)^2} p(i, j), \quad (3)$$

were calculated to respectively characterize the intensity heterogeneity, symmetry, and structural isotropy of the fibers, where

$$\mu_i = \sum_{i=0}^{g-1} \sum_{j=0}^{g-1} i \cdot p(i, j), \quad (4)$$

$$\mu_j = \sum_{i=0}^{g-1} \sum_{j=0}^{g-1} j \cdot p(i, j) \quad (5)$$

[38].

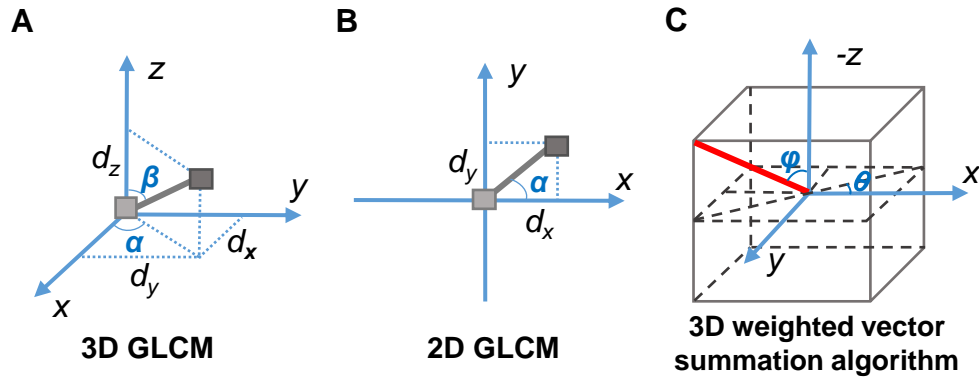


Fig. 1. Definitions of key parameters involved in image analysis. (A, B) Parameters determining the relative positions of (A) a pair of voxels in 3D GLCM or (B) a pair of pixels in 2D GLCM algorithms. (C) Parameters determining the spatial fiber orientation in 3D weighted vector summation algorithm. The red solid line represents the fiber of interest. GLCM: gray level co-occurrence matrix.

For comparison, 2D GLCM analysis was also performed. The principle of the 2D GLCM algorithm is exactly the same as the 3D GLCM, except for the dimensionality reduction. Owing to the reduced dimension, the distance $|\vec{d}|$ is only determined by d_x and d_y , and the direction is only specified by α in 2D GLCM (Fig. 1(B)).

For 3D GLCM analysis, the three texture features mentioned above were calculated with a $|\vec{d}|$ of 3, 4, 5, and 6 voxels and a (α, β) of $(0^\circ, 45^\circ)$, $(0^\circ, 135^\circ)$, $(-, 0^\circ)$, $(45^\circ, 45^\circ)$, $(45^\circ, 135^\circ)$, $(90^\circ, 45^\circ)$, $(90^\circ, 135^\circ)$, $(135^\circ, 45^\circ)$, and $(135^\circ, 135^\circ)$. Here, “-” denotes arbitrary angle. For 2D GLCM analysis, the three features were calculated with a $|\vec{d}|$ of 3, 4, 5, and 6 pixels and an α of 0° , 45° , 90° , and 135° . For a given texture feature, the results obtained with different distances and directions were averaged to obtain the final quantitative value for subsequent statistics, comparisons, and classification. All of the above calculations and analyses were performed using MATLAB (MathWorks) programming.

2.5. Spatial orientation analysis based on 3D weighted vector summation algorithm

To quantify the voxel-wise orientation of collagen and elastin fibers within the normal and CAP-lesioned inner arterial walls, a 3D weighted vector summation algorithm was adopted. Details of the algorithm can be found in a previous paper [27]. Initially, an approximately cubic window is created in a 3D image to evaluate the orientation of each voxel within the window. Then, for a given voxel, the algorithm defines all the possible vectors passing through the voxel, weighs each vector according to the variability of voxel intensities along the vector, and finally sums up these weighted vectors to obtain the orientation. An azimuthal angle θ in the transverse

plane and an inclination angle φ are defined to depict the orientation in the 3D space, as shown in Fig. 1(C). To cover all the 3D orientations, both θ and φ vary in the range of 0° to 180° . Note that $\varphi = 90^\circ$ indicates that the fibers are parallel to the optical sections, and for the 2D case, a single angle θ is sufficient to depict the fiber orientation [27].

In this study, a window with a size of $9 \times 9 \times 5$ voxels ($11 \times 11 \times 15 \mu\text{m}^3$) was created to calculate the voxel-wise 3D fiber orientation. Color-coded θ and φ orientation maps were generated to visually illustrate the obtained orientation. Moreover, the 3D directional variance [28] that measures the orientation dispersion degree of an image stack was calculated to quantify the overall fiber alignment. A lower 3D directional variance value reveals more highly aligned fibers, while a higher one corresponds to a more random fiber alignment.

2.6. Multivariate classification model

To realize automatic and robust discrimination of normal tissue and CAP lesions, we established a binary classification model by integrating complementary microstructural information provided by the 3D GLCM and 3D weighted vector summation algorithm. Considering the small sample size used in this study, the linear SVM algorithm [39] was utilized. Four preferential 3D quantitative microstructural features, including *entropy*, *cluster shade*, *homogeneity*, and 3D directional variance, of both collagen and elastin fibers (total of eight features) were chosen as candidates for constructing the SVM classifier. To obtain the optimal classifier, we evaluated the contribution of the eight features by screening SVM classifiers constructed based on all possible combinations of the features. The leave-one-out cross-validation method [40] which is suitable for datasets with small sizes, was used to evaluate the accuracy, sensitivity, and specificity of the SVM classifier, based on the comparison between the test results and the standard histopathological diagnosis. By plotting the true positive rate against the false positive rate, a receiver operator characteristic (ROC) curve [41] was obtained, and the area under the curve (AUC) value, which is a composite of accuracy, sensitivity, and specificity, was calculated. The AUC value was taken as the ultimate evaluation criterion of the classifier's performance to screen out the optimal combination of the microstructural features and to obtain the best SVM classifier.

2.7. Statistical analysis

Statistical analyses were performed using GraphPad Prism software (GraphPad Software). For quantitative comparison of normal and CAP-lesion groups (paired data were obtained from each patient by averaging results of multiple normal or CAP regions), a two-tailed paired t test was used, and differences were considered to be statistically significant for $P < 0.05$.

3. Results and discussion

3.1. MPM imaging reveals microstructures of fibers in normal and CAP lesioned coronary artery

To assess the ability of MPM imaging in revealing the histological characteristics of the artery for CAP identification, we first captured a MPM image of an intact CAP and the surrounding tissue, by performing 3D large-FOV MPM imaging on a cross section of the human coronary artery wall. It is well known that the artery wall generally consists of three layers: the tunica intima, tunica media, and tunica adventitia. The internal and external boundaries of the tunica media can be roughly delineated by the inner and external elastic membranes, respectively [42]. As expected, the typical imaging result (Fig. 2, imaging volume: $2.45 \text{ mm} \times 1.48 \text{ mm} \times 48 \mu\text{m}$) shows that the distribution and the microstructures of collagen and elastin fibers were revealed by the SHG and TPEF signals, respectively. The internal and external elastic membranes could be easily discriminated based on their unique features of linear structure and dense elastin. Demarcated

by the two membranes, the three layers that make up the artery wall were clearly identified. Furthermore, the CAP was identified by the relatively disorganized collagen and elastin fibers, compared to the surrounding tissues, and the obvious intimal hyperplasia observed around it (Fig. 2). These findings demonstrate that cross-sectional large-FOV MPM imaging can reveal differences in the fiber structures of the CAP and the neighboring tissues in a label-free manner.

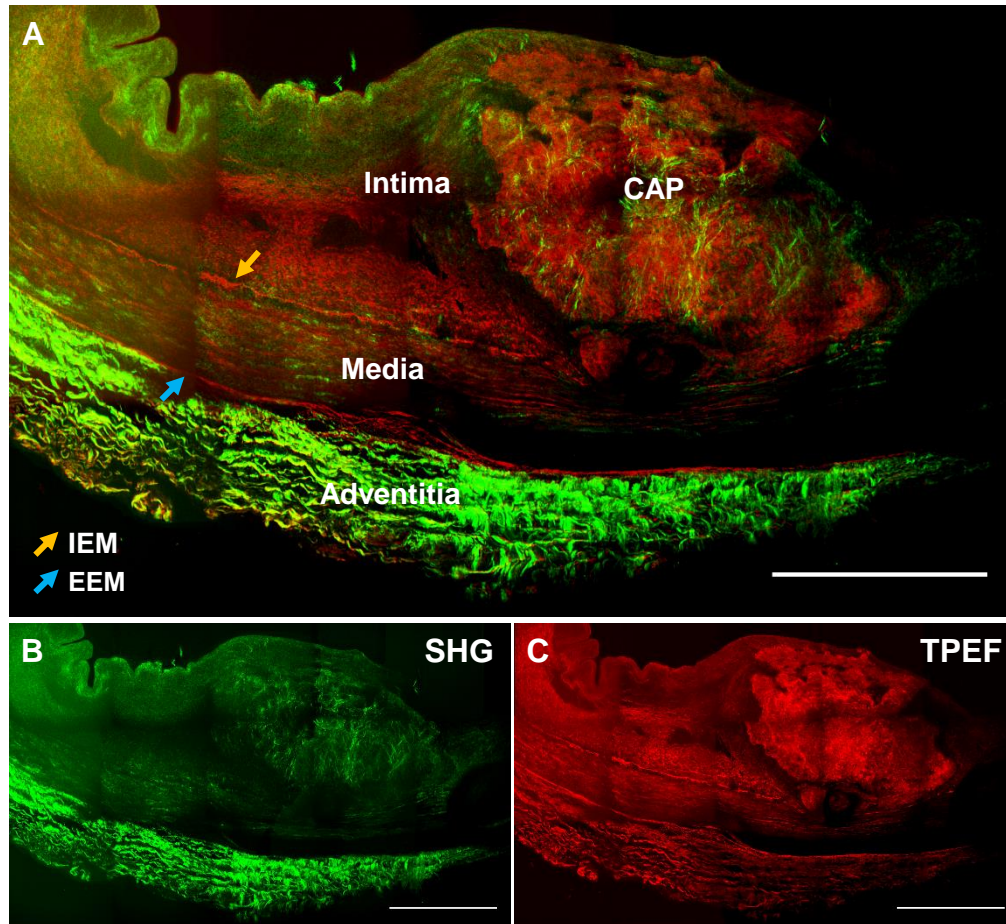


Fig. 2. 3D large-field-of-view MPM imaging on the cross section of human artery wall draws a general picture of the fiber structures within CAP and surrounding tissues. (A) Merged image of (B) SHG (collagen fibers) and (C) TPEF (dominated by elastin fibers) signals. All the images are projections along the z axis, and the covered imaging depth is 48 μm . Scale bar: 500 μm . CAP: coronary atherosclerotic plaque; IEM: internal elastic membrane; EEM: external elastic membrane.

As the ultimate goal of MPM imaging for CAP assessment is *in vivo* “optical biopsy”, we further evaluated if angioscopy-view MPM imaging has CAP-discerning ability comparable to that of cross-sectional large-FOV MPM imaging. The obtained 3D en face single-FOV MPM images (Fig. 3(A)) show that the collagen and elastin fibers within the normal inner arterial wall are orderly arranged with uniform texture and consistent orientation. By contrast, a slight disruption of the collagen and elastin fibers was observed in the neighboring CAP region in the form of boundary-blurred collagen fibers and partially fragmented elastin fibers. These microstructural features are consistent with what has been observed in traditional histological

sections (Fig. 3(B)) and the large-FOV MPM image of the artery-wall cross section (Fig. 2). The action of proteolytic enzymes during CAP development might be the major cause of the aforementioned alterations in arterial fibers [10,43]. Furthermore, by merging the SHG and the TPEF images, we found that the CAP tissue has a remarkably lower ratio of TPEF to SHG, compared with the neighboring normal inner arterial wall (Fig. 3(A)). We further confirmed this observation by quantitative spectral analysis (Fig. 3(C) and 3(D)). This might be a result of increased collagen synthesis by smooth muscle cells that migrate into the tunica intima during CAP formation [44,45]. These results demonstrate that en face single-FOV MPM imaging is adequate for capturing the differences in fiber structure and content between the normal artery wall and the CAP tissue, thus showing great potential as an *in vivo* “optical biopsy” tool for CAP assessment.

Besides, it is worth noting that the TPEF signals doesn't completely originate from the elastin fibers, but it is certainly dominated by the elastin signal in this study. Because among the various tissue components of normal artery wall and CAP [1,42], only the cells and the elastin fibers can emit distinct two-photon excitation autofluorescence at 790 nm or 810 nm excitation wavelength that we used. Whereas the two-photon excitation autofluorescence of cells was greatly attenuated by the sample preparation procedures, especially PFA fixation, since the signal is metabolism-related [17]. In addition, the TPEF signal forms obvious fibrous structures (Fig. 3(A)) and shows emission spectrum (Fig. 3(C)) consistent with that of the elastin [16]. Therefore, we equated TPEF signal to the elastin signal hereafter for convenient description.

3.2. 3D GLCM quantifies spatial texture features of collagen and elastin fibers

To further realize quantitative CAP identification, we extracted spatial texture features of collagen and elastin fibers within CAP and the normal inner arterial wall using the 3D GLCM algorithm. We calculated a total of 12 texture features, including *energy*, *entropy*, *correlation*, *contrast*, *variance*, *sum mean*, *inertia*, *cluster shade*, *cluster tendency*, *homogeneity*, *maximum probability*, and *inverse variance* [36]. Comparative analysis revealed that the difference between the normal artery wall and the CAP tissue is statistically significant in three of the 12 texture features: *entropy*, *cluster shade*, and *homogeneity*. The three features characterize the intensity heterogeneity, symmetry, and structural isotropy of the fibers, respectively. As shown in Fig. 4, a lower value of *entropy* and higher values of *cluster shade* and *homogeneity* relative to the normal inner arterial wall were derived from the CAP tissue for both collagen and elastin fibers. The results demonstrate that the fiber texture of both CAP and normal inner arterial wall captured by MPM imaging can be successfully quantified by typical 3D GLCM features, and these features show the potential to be utilized as indicators for CAP identification.

In addition, we performed 2D GLCM analysis for comparison. Typically, 2D GLCM takes the average value of features obtained from different depths or the feature value calculated at a certain imaging depth as a representative analysis result. Thus, we calculated the aforementioned three texture features, *entropy*, *cluster shade*, and *homogeneity* at each imaging depth with parameters equivalent to those used in 3D GLCM analysis for fair comparison. Taking elastin fiber as an example, significant fluctuations were observed in the values of texture features as the imaging depth increased, which made it difficult to discriminate CAP from normal tissues (Fig. 5). This result indicates that the 2D GLCM analysis essentially correlates with the selection of imaging depth, which may lead to remarkably decreased accuracy and repeatability of CAP evaluation, compared with the 3D GLCM analysis.

3.3. 3D weighted vector summation algorithm quantifies spatial orientation features of collagen and elastin fibers

In addition to the texture features, the spatial orientation features of collagen and elastin fibers were derived using the 3D weighted vector summation algorithm to provide complementary

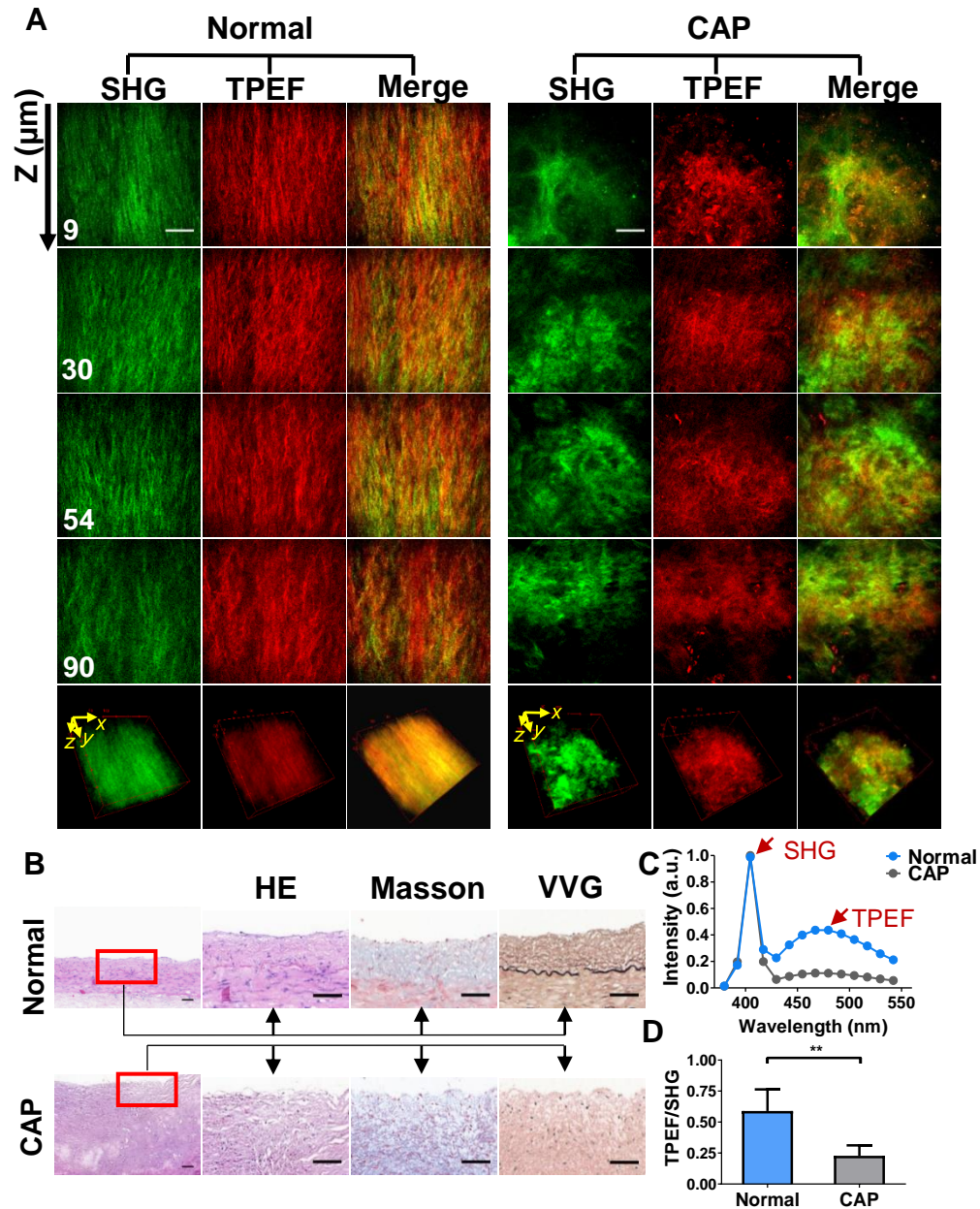


Fig. 3. 3D single-field-of-view MPM imaging from the perspective of angioscopes reveals the microstructures and the relative content of collagen and elastin fibers within the normal and CAP lesioned human coronary artery. (A) SHG (collagen fibers), TPEF (dominated by elastin fibers), and merged images. The digit labeled at the bottom left corner of each panel indicates the depth. (B) H&E, Masson (for collagen), and VVG (for elastin) stained histology images. (C) Emission spectra corresponding to (A). (D) Intensity ratio of TPEF to SHG. The value was calculated using the emission-peak intensities as indicated by red arrows shown in (C). The error bars denote the SEM. **: $0.001 < P < 0.01$, two-tailed paired t test. Scale bars: $60 \mu\text{m}$.

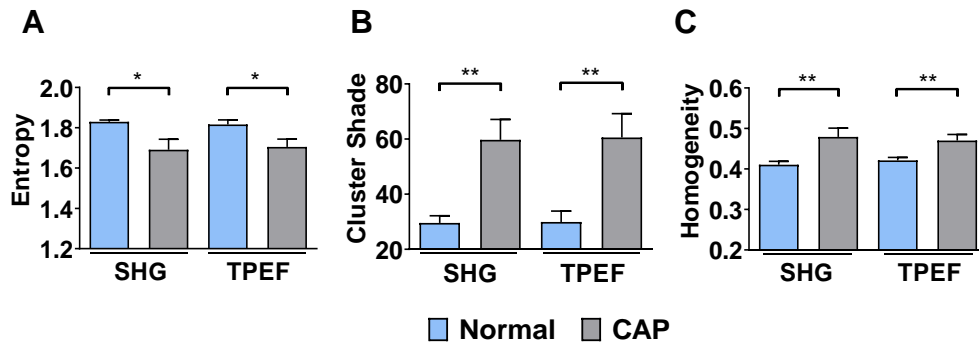


Fig. 4. Spatial texture features (A) *entropy*, (B) *cluster shade*, and (C) *homogeneity* of fibers derived from the 3D GLCM show significant differences between normal and CAP tissues. The error bars denote the standard error of mean (SEM). **: $0.001 < P < 0.01$; * $P < 0.05$, two-tailed paired t test.

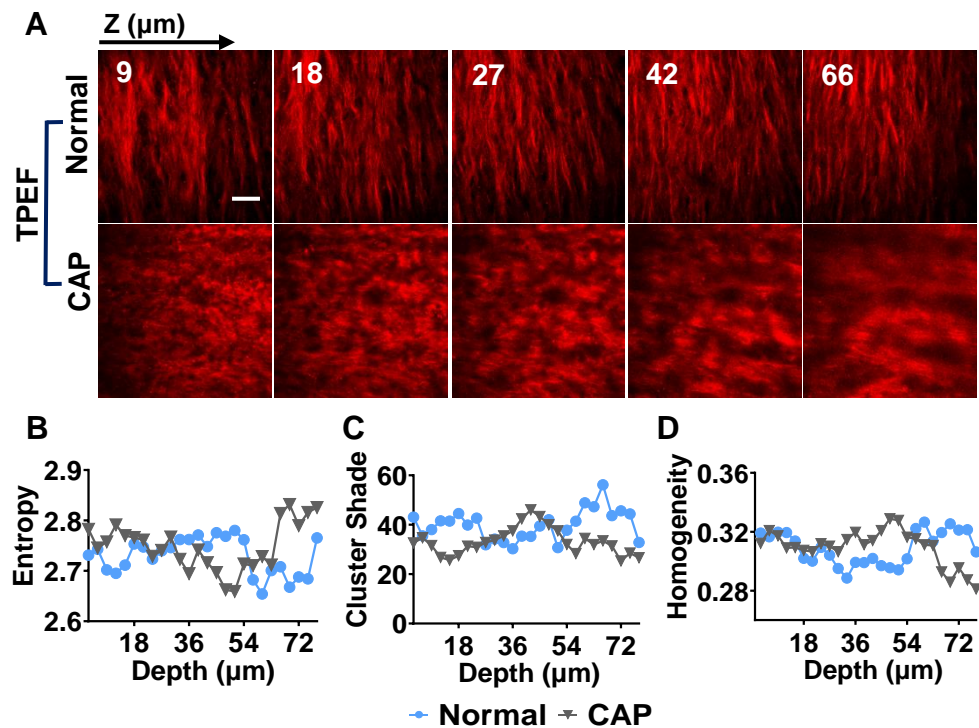


Fig. 5. 2D GLCM texture features fluctuate along the imaging depth, resulting in an inadequate capacity of discerning CAP. (A) Typical TPEF (dominated by elastin fibers) images of a normal region and the neighboring CAP region. The digit labeled at the top left corner of each panel indicates the depth. (B-D) 2D GLCM texture features: (B) *entropy*, (C) *cluster shade*, and (D) *homogeneity* derived from (A) are presented as functions of depth. Scale bar: 60 μm .

quantitative indicators for CAP identification. Here, an azimuthal angle θ in the transverse plane and an inclination angle φ are calculated and combined to depict the voxel-wise 3D orientation of fibers.

For collagen fibers visualized by SHG imaging, a relatively uniform θ orientation in the normal inner arterial wall was revealed by color-coded orientation maps with a predominant color of green to yellow and a probability density distribution with a distinct peak at $\sim 90^\circ$. Contrastingly, a nearly random distribution of the θ orientation was observed in the CAP tissue (Fig. 6(A) and 6(B)). In terms of the φ orientation, the color-coded orientation maps show some features of depth dependency, especially for the normal group (Fig. 6(A)). This reflects the wavy structure of the fibers and shows potential for quantifying the size and period of fiber waves. The probability density distributions of φ revealed broadly similar fiber orientation features in the normal inner arterial wall and the CAP in general (Fig. 6(A) and 6(C)). Note that a peak at $\sim 90^\circ$ of φ orientation was observed in both groups (Fig. 6(C)), indicating that the collagen fibers were still arranged nearly parallel to the inner-surface of the artery wall when a CAP lesion occurred. Furthermore, the overall fiber alignment was quantified by a 3D directional variance of the voxel-wise orientations, and a paired comparison was performed. A higher value was derived from the CAP lesion when compared to the normal tissue for every patient, and the overall difference was statistically significant (Fig. 6(D)), suggesting that the feature of 3D fiber orientation is robust enough to be a CAP indicator. Similar analysis results were obtained for elastin fibers visualized by TPEF imaging (Fig. 7).

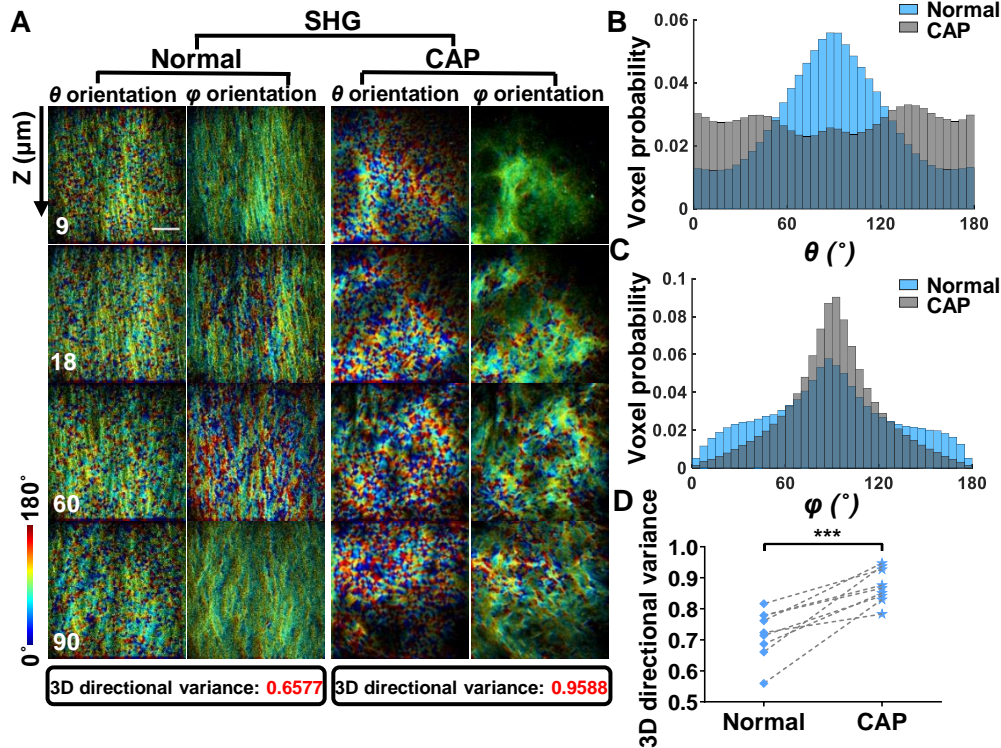


Fig. 6. Spatial orientation features of collagen fibers quantified by the 3D weighted vector summation algorithm show significant differences between normal and CAP tissues. (A) Color-coded θ and φ orientation maps. The digit labeled at the bottom left corner of each panel indicates the depth. The corresponding 3D directional variances are given below the figures. (B, C) Probability density distributions of (B) θ and (C) φ orientations. (D) 3D directional variance presented in the form of paired comparison. The two data points connected with a dashed line are from the same specimen. ***: $P < 0.001$, two-tailed paired t test. Scale bar: 60 μm .

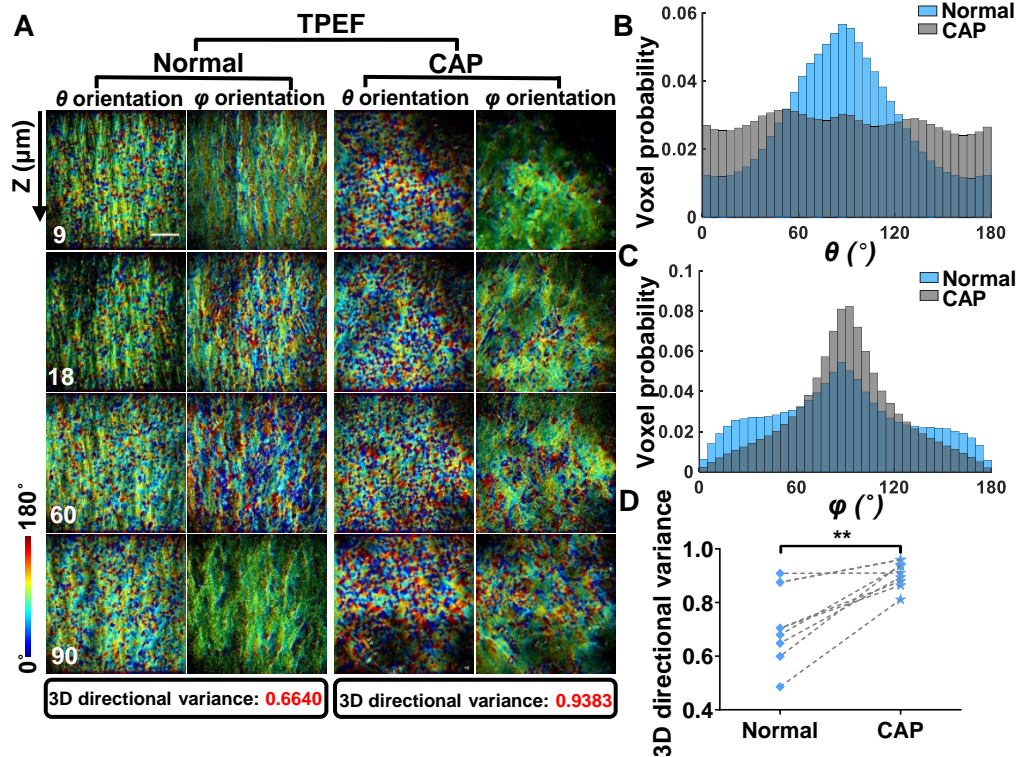


Fig. 7. Spatial orientation features of elastin fibers quantified by the 3D weighted vector summation algorithm show significant differences between normal and CAP tissues. (A) Color-coded θ and φ orientation maps. The digit labeled at the bottom left corner of each panel indicates the depth. The corresponding 3D directional variances are given below the figures. (B, C) Probability density distributions of θ and φ orientations. (D) 3D directional variance presented in the form of paired comparison. The two data points connected with a dashed line are from the same specimen. **: $0.001 < P < 0.01$, two-tailed paired t test. Scale bar: 60 μm .

It should be stressed that for fibers in both the normal inner arterial wall and CAP tissue, a common case is that the φ orientation map varies with the imaging depth, while similar θ orientation maps are acquired from all the depths (Figs. 6(A), 7(A), and 8). In this case, 2D analysis that uses a single angle θ to depict the fiber orientation cannot reveal the 3D distribution of the fiber spatial orientation, even on integrating the results obtained at every imaging depth. By contrast, the 3D weighted vector summation algorithm can easily achieve comprehensive and detailed characterization of fiber spatial orientations. Benefitting from its voxel-wise quantification ability, the method would not only contribute to CAP identification but also provide an indispensable indicator for the early stage evaluation and risk assessment of CAP, when combined with MPM.

In addition to the typical result that fibers within the normal inner arterial wall present a nearly uniform θ orientation at different depths as shown above (Figs. 6(A), 7(A), and 8A), we captured variable θ orientations in some of the nine cases (an example is shown in Fig. S1 and S2 in Supplement 1). This is expected because the imaging may not only cover the tunica intima but also the tunica media of the artery wall. The tunica intima has a generally uniform fiber orientation, but its thickness varies widely from patient to patient, owing to the individual differences among them, especially in gender and age. Contrastingly, the fiber orientation of

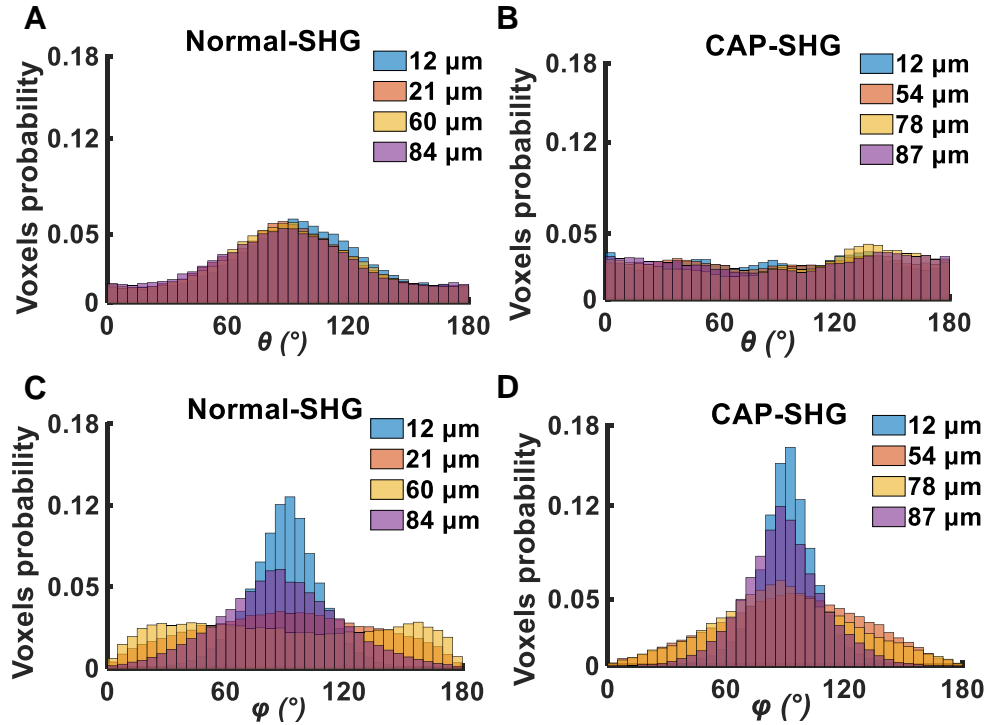


Fig. 8. Probability density distributions of (A, B) θ and (C, D) φ orientations of collagen fibers at different depths suggests that the 3D orientation distribution cannot be revealed by integrating 2D orientations at every imaging depth. Different colors represent results obtained at different depths as indicated at the top right corner of each panel.

tunica media gradually changes with depth [46,47]. Nonetheless, it is certain that the CAP shows a more random fiber orientation than the normal inner arterial wall in general, and this feature can be successfully derived from MPM imaging and further quantified by the 3D directional variance (Figs. 6(D) and 7(D)).

3.4. SVM classification model integrating multivariate 3D microstructural features

The quantitative and stereo microstructural features, including *entropy*, *cluster shade*, *homogeneity*, and 3D directional variance, of arterial fibers can be used as indicators for CAP identification, as they are demonstrated to be significantly different in the normal artery and CAP. However, owing to individual differences among patients, it is difficult to realize automatic and robust CAP identification by merely relying on the value of a single microstructural feature.

To realize the full potential of 3D fiber microstructures in clinical diagnosis, we established a SVM classification model by integrating the four preferential texture and orientation features to discriminate the normal inner arterial wall from the CAP. Considering the ROC AUC value as the indicator of SVM classifier performance, we first screened all possible combinations of these features separately for collagen and elastin fibers. For both types of fibers, we finalized a combination of *entropy* and 3D directional variance as the optimal one (Figs. 9(A) and 9(B), Table 1). Furthermore, by integrating the features of collagen and elastin fibers and performing similar screening as above, a combination of *entropy* of collagen fibers, *entropy* of elastin fibers, and 3D directional variance of collagen fibers was selected to construct the best SVM

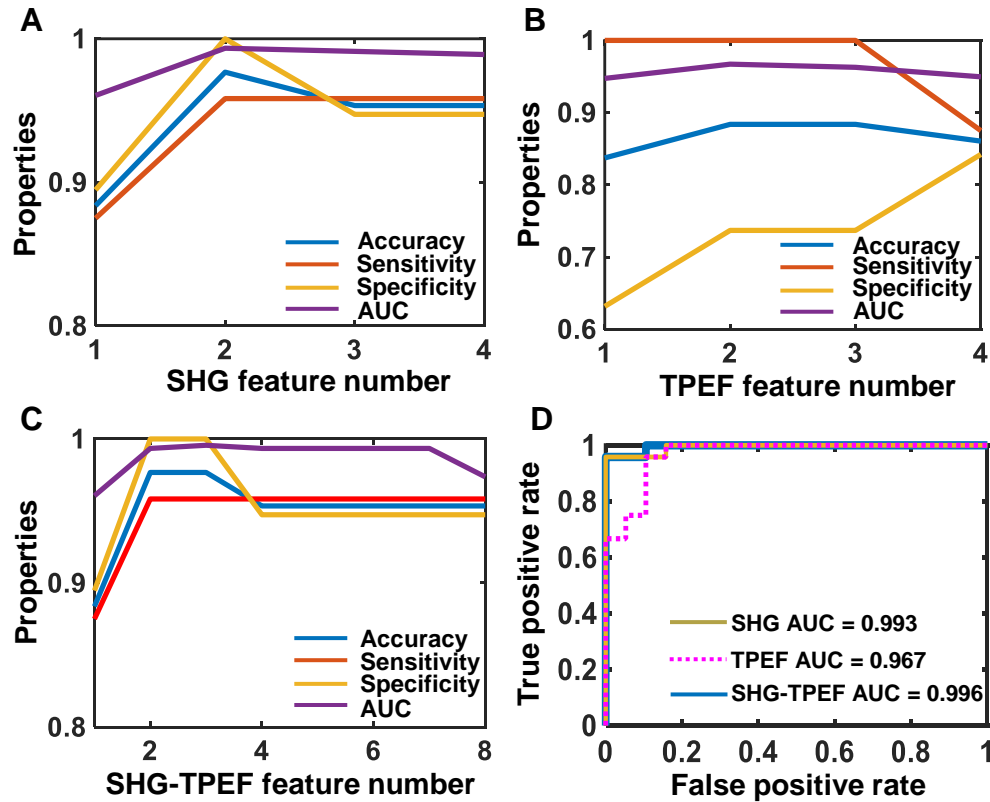


Fig. 9. By integrating preferential 3D texture and orientation features of artery intima fibers, the SVM classification model discriminates the CAP from normal tissue with an accuracy of >97%. (A-C) Performance of SVM classifiers constructed based on different number of microstructural features that were derived from (A) collagen fibers (SHG), (B) elastin fibers (TPEF), and (C) combination of collagen and elastin fibers (SHG-TPEF). For a given number of features, we only show the result of the best classifier. (D) ROC curves of SVM classifiers with best performance which were screened out from (A-C).

classifier (Fig. 9(C), Table 1). Classification accuracies of 97.7%, 88.4%, and 97.7% were achieved using the optimal SVM classifiers constructed based on collagen fibers, elastin fibers, and integration of collagen and elastin fibers, respectively, with AUC values of 0.993, 0.967, and 0.996 (Fig. 9(D), Table 1). The collagen-based classifier showed remarkably better performance than the elastin-based classifier, while it was slightly inferior to the collagen-elastin-based classifier, which achieved a relatively higher sensitivity and AUC value (Fig. 9(D), Table 1). These results demonstrate that the 3D-fiber-microstructure-based SVM classifiers, especially the collagen-based classifier and the collagen-elastin-based classifier, show promising prospects in clinical CAP assessment.

Table 1. Performance of optimal SVM classifiers constructed based on SHG, TPEF, and combination of SHG and TPEF images

	SHG	TPEF	SHG–TPEF
Accuracy	97.7%	88.4%	97.7%
Sensitivity	95.8%	100%	95.9%
Specificity	100%	73.7%	100%
Features	Entropy, 3D directional variance	Entropy, 3D directional variance	SHG entropy, TPEF entropy, SHG 3D directional variance

4. Conclusions

In summary, by combining endogenous MPM signal detection with 3D image analysis algorithms, we proposed a label-free approach for CAP identification using the spatial microstructural features of arterial fibers as quantitative indicators. Based on human coronary artery specimens, we showed that the microstructures of collagen and elastin fibers within the normal artery wall and CAP tissue can be captured by MPM imaging from the perspective of angioscopes, without applying any exogenous contrast agent. Furthermore, we demonstrated that 3D GLCM and 3D weighted vector summation algorithms can easily achieve comprehensive and detailed quantification of the spatial texture and orientation features of arterial fibers, and these features show potential as indicators for CAP identification. Finally, by using a combination of the extracted quantitative microstructural features, we established a SVM-based classification model with an accuracy >97%, which is promising for providing fully automated CAP identification. Because of the difficulty in specimen collection, we only demonstrated the viability of the proposed method for the general identification of human CAP. Nonetheless, the micron-level characterization and automatic discrimination abilities of the method may allow early stage evaluation, risk assessment, and multi-stage differentiation of CAP, which will be demonstrated in our future work. There is an increasing interest in the development of multiphoton endoscopes for clinical use [48,49]. These advances will lead to the miniaturization of the MPM in the future for minimally invasive, label-free, quantitative, and real-time identification and risk assessment of CAP based on the proposed method.

Funding. National Key Research and Development Program of China (2017YFC0110200, 2019YFE0113700); National Natural Science Foundation of China (81822023, 91959121, 82071972, 61905214); Guangdong Provincial Key Laboratory of Biomedical Optical Imaging (2020B121201010); Guangdong Basic and Applied Basic Research Foundation (2019A1515011746, 2019A1515111182); Science and Technology Planning Project of Guangdong Province (2016B070701007); Shenzhen Basic Research Program (JCYJ20170818164343304, JCYJ20180507182432303); Shenzhen Key Laboratory for Molecular Imaging (ZDSY20130401165820357); CAS Key Laboratory of Health Informatics, Shenzhen Institute of Advanced Technology (2011DP173015); High-level Hospital Construction Project of Guangdong Provincial People's Hospital (DFJH201904).

Disclosures. The authors declare on conflicts of interest.

Supplemental document. See [Supplement 1](#) for supporting content.

References

1. D. Steinberg and A. M. Gotto, "Preventing coronary artery disease by lowering cholesterol levels - fifty years from bench to bedside," *JAMA* **282**(21), 2043–2050 (1999).
2. D. E. Gutstein and V. Fuster, "Pathophysiology and clinical significance of atherosclerotic plaque rupture," *Cardiovasc. Res.* **41**(2), 323–333 (1999).
3. P. R. Moreno, E. Falk, I. F. Palacios, J. B. Newell, V. Fuster, and J. T. Fallon, "Macrophage infiltration in acute coronary syndromes. Implications for plaque rupture," *Circulation* **90**(2), 775–778 (1994).
4. P. Libby, "Changing concepts of atherogenesis," *J. Intern. Med.* **247**(3), 349–358 (2000).
5. B. K. Courtney, N. R. Munce, K. J. Anderson, A. S. Thind, G. Leung, P. E. Radau, F. S. Foster, I. A. Vitkin, R. S. Schwartz, A. J. Dick, G. A. Wright, and B. H. Strauss, "Innovations in imaging for chronic total occlusions: a glimpse into the future of angiography's blind-spot," *Eur. Heart. J.* **29**(5), 583–593 (2008).
6. P. G. Yock and P. J. Fitzgerald, "Intravascular ultrasound: state of the art and future directions," *Am. J. Cardiol.* **81**(7), 27E–32E (1998).

7. J. M. Hodgson, K. G. Reddy, R. Suneja, R. N. Nair, E. J. Lesnefsky, and H. M. Sheehan, "Intracoronary ultrasound imaging: correlation of plaque morphology with angiography, clinical syndrome and procedural results in patients undergoing coronary angioplasty," *J. Am. Coll. Cardiol.* **21**(1), 35–44 (1993).
8. L. B. Mostaco-Guidolin, E. K. Kohlenberg, M. Smith, M. Hewko, A. Major, M. G. Sowa, and A. C. T. Ko, "Quantitative nonlinear optical assessment of atherosclerosis progression in rabbits," *Anal. Chem.* **86**(13), 6346–6354 (2014).
9. K. J. Ransohoff and J. C. Wu, "Advances in cardiovascular molecular imaging for tracking stem cell therapy," *Thromb. Haemostasis* **104**(07), 13–22 (2010).
10. P. Libby, P. M. Ridker, and G. K. Hansson, "Progress and challenges in translating the biology of atherosclerosis," *Nature* **473**(7347), 317–325 (2011).
11. J. A. Jo, J. Park, P. Pande, S. Shrestha, M. J. Serafino, J. D. R. Jimenez, F. Clubb, B. Walton, L. M. Buja, J. E. Phipps, M. D. Feldman, J. Adame, and B. E. Applegate, "Simultaneous morphological and biochemical endogenous optical imaging of atherosclerosis," *Eur. Heart. J.-Card. Img.* **16**(8), 910–918 (2015).
12. R. Virmani, A. P. Burke, A. Farb, and F. D. Kolodgie, "Pathology of the vulnerable plaque," *J. Am. Coll. Cardiol.* **47**(8), C13–C18 (2006).
13. E. V. Gubarkova, V. V. Dudenkova, F. I. Feldchtein, L. B. Timofeeva, E. B. Kiseleva, S. S. Kuznetsov, B. E. Shakhov, A. A. Moiseev, V. M. Gelikonov, G. V. Gelikonov, A. Vitkin, and N. D. Gladkova, "Multi-modal optical imaging characterization of atherosclerotic plaques," *J. Biophotonics* **9**(10), 1009–1020 (2016).
14. T. T. Le, I. M. Langohr, M. J. Locker, M. Sturek, and J. X. Cheng, "Label-free molecular imaging of atherosclerotic lesions using multimodal nonlinear optical microscopy," *J. Biomed. Opt.* **12**(5), 054007 (2007).
15. X. Li, H. Li, X. Z. He, T. G. Chen, X. Y. Xia, C. X. Yang, and W. Zheng, "Spectrum- and time-resolved endogenous multiphoton signals reveal quantitative differentiation of premalignant and malignant gastric mucosa," *Biomed. Opt. Express* **9**(2), 453–471 (2018).
16. A. Zoumi, X. A. Lu, G. S. Kassab, and B. J. Tromberg, "Imaging coronary artery microstructure using second-harmonic and two-photon fluorescence microscopy," *Biophys. J.* **87**(4), 2778–2786 (2004).
17. W. R. Zipfel, R. M. Williams, R. Christie, A. Y. Nikitin, B. T. Hyman, and W. W. Webb, "Live tissue intrinsic emission microscopy using multiphoton-excited native fluorescence and second harmonic generation," *P. Natl. Acad. Sci. U. S. A.* **100**(12), 7075–7080 (2003).
18. S. Gorovitz and A. MacIntyre, "Toward a theory of medical fallibility," *Hastings Cent. Rep.* **5**(6), 13–23 (1975).
19. R. Cicchi, E. Baria, C. Matthaus, M. Lange, A. Lattermann, B. R. Brehm, J. Popp, and F. S. Pavone, "Non-linear imaging and characterization of atherosclerotic arterial tissue using combined SHG and FLIM microscopy," *J. Biophotonics* **8**(4), 347–356 (2015).
20. R. Cicchi, C. Matthaus, T. Meyer, A. Lattermann, B. Dietzek, B. R. Brehm, J. Popp, and F. S. Pavone, "Characterization of collagen and cholesterol deposition in atherosclerotic arterial tissue using non-linear microscopy," *J. Biophotonics* **7**(1-2), 135–143 (2014).
21. E. Baria, G. Nesi, R. Santi, V. Maio, D. Massi, C. Pratesi, R. Cicchi, and F. S. Pavone, "Improved label-free diagnostics and pathological assessment of atherosclerotic plaques through nonlinear microscopy," *J. Biophotonics* **11**(11), e201800106 (2018).
22. A. Depeursinge, A. Foncubierta-Rodriguez, D. V. De Ville, and H. Muller, "Three-dimensional solid texture analysis in biomedical imaging: Review and opportunities," *Med. Image. Anal.* **18**(1), 176–196 (2014).
23. R. M. Haralick, K. Shanmugam, and I. Dinstein, "Textural features for image classification," *IEEE Trans. Syst., Man, Cybern.* **SMC-3**(6), 610–621 (1973).
24. W. Chen, M. L. Giger, H. Li, U. Bick, and G. M. Newstead, "Volumetric texture analysis of breast lesions on contrast-enhanced magnetic resonance images," *Magn. Reson. Med.* **58**(3), 562–571 (2007).
25. T. Y. Kim, N. H. Cho, G. B. Jeong, E. Bengtsson, and H. K. Choi, "3D texture analysis in renal cell carcinoma tissue image grading," *Comput. Math. Method. M.* **2014**, 1–12 (2014).
26. K. Kothavari, B. Arunadevi, and S. N. Deepa, "A hybrid DE-RGSO-ELM for brain tumor tissue categorization in 3D magnetic resonance images," *Math. Probl. Eng.* **2014**, 1–14 (2014).
27. Z. Y. Liu, K. P. Quinn, L. Speroni, L. Arendt, C. Kuperwasser, C. Sonnenschein, A. M. Soto, and I. Georgakoudi, "Rapid three-dimensional quantification of voxel-wise collagen fiber orientation," *Biomed. Opt. Express* **6**(7), 2294–2310 (2015).
28. Z. Y. Liu, D. Pouli, D. Sood, A. Sundarakrishnan, C. K. H. Mingalone, L. M. Arendt, C. Alonzo, K. P. Quinn, C. Kuperwasser, L. Zeng, T. Schnellendorfer, D. L. Kaplan, and I. Georgakoudi, "Automated quantification of three-dimensional organization of fiber-like structures in biological tissues," *Biomaterials* **116**, 34–47 (2017).
29. Z. Y. Liu, L. Arendt, D. Pouli, C. Kuperwasser, and I. Georgakoudi, "Quantification of three-dimensional collagen fiber organization as a sensitive indicator of cancerous changes," *Cancer Res.* **77**, B17 (2017).
30. Z. Y. Liu, L. Speroni, K. P. Quinn, C. Alonzo, D. Pouli, Y. Zhang, E. Stuntz, C. Sonnenschein, A. M. Soto, and I. Georgakoudi, "3D organizational mapping of collagen fibers elucidates matrix remodeling in a hormone-sensitive 3D breast tissue model," *Biomaterials* **179**, 96–108 (2018).
31. H. C. Strydom, D. H. Blankenhorn, A. B. Chandler, S. Glagov, W. Insull, M. Richardson, M. E. Rosenfeld, S. A. Schaffer, C. J. Schwartz, W. D. Wagner, and R. W. Wissler, "A definition of the intima of human arteries and of its atherosclerosis-prone regions - a report from the committee on vascular-lesions of the council on arteriosclerosis, American-Heart-Association," *Circulation* **85**(1), 391–405 (1992).

32. U. Michael, "Stack Focuser," <https://imagej.nih.gov/ij/plugins/stack-focuser.html>.
33. C. Blasse, S. Saalfeld, R. Etournay, A. Sagner, S. Eaton, and E. W. Myers, "PreMosa: extracting 2D surfaces from 3D microscopy mosaics," *Bioinformatics* **33**(16), 2563–2569 (2017).
34. H. Li, Q. Cui, Z. H. Zhang, L. Fu, and Q. M. Luo, "Nonlinear optical microscopy for immunoimaging: a custom optimized system of high-speed, large-area, multicolor imaging," *Quant. Imag. Med. Surg.* **5**, 30–39 (2015).
35. S. K. Teh, W. Zheng, S. X. Li, D. Li, Y. Zeng, Y. Q. Yang, and J. A. Y. Qu, "Multimodal nonlinear optical microscopy improves the accuracy of early diagnosis of squamous intraepithelial neoplasia," *J. Biomed. Opt.* **18**(3), 036001 (2013).
36. C. Philips, D. Li, J. Furst, and D. Raicu, "An analysis of co-occurrence and gabor texture classification in 2D and 3D," Proceedings for CARS (2008).
37. A. S. Kurani, D. H. Xu, J. Furst, and D. S. Raicu, "Co-occurrence matrices for volumetric data," *Heart* **27**, 25 (2004).
38. X. F. Yang, S. Tridandapani, J. J. Beitler, D. S. Yu, E. J. Yoshida, W. J. Curran, and T. Liu, "Ultrasound GLCM texture analysis of radiation-induced parotid-gland injury in head-and-neck cancer radiotherapy: An in vivo study of late toxicity," *Med. Phys.* **39**(9), 5732–5739 (2012).
39. C. Cortes and V. Vapnik, "Support-vector networks," *Mach Learn* **20**(3), 273–297 (1995).
40. Z. E. Maglogiannis I and I. Anagnostopoulos, "An intelligent system for automated breast cancer diagnosis and prognosis using SVM based classifiers," *Appl Intell* **30**(1), 24–36 (2009).
41. D. H. Lee, X. Li, N. Ma, M. A. Digman, and A. P. Lee, "Rapid and label-free identification of single leukemia cells from blood in a high-density microfluidic trapping array by fluorescence lifetime imaging microscopy," *Lab Chip* **18**(9), 1349–1358 (2018).
42. "The cardiovascular system: blood vessels and circulation," *Anatomy and Physiology* (OpenStax, 2013), pp. 844–855.
43. A. C. Newby, "Dual role of matrix metalloproteinases (matrixins) in intimal thickening and atherosclerotic plaque rupture," *Physiol. Rev.* **85**(1), 1–31 (2005).
44. H. C. Sary, A. B. Chandler, R. E. Dinsmore, V. Fuster, S. Glagov, W. Insull, M. E. Rosenfeld, C. J. Schwartz, W. D. Wagner, and R. W. Wissler, "A definition of advanced types of atherosclerotic lesions and a histological classification of atherosclerosis - a report from the committee on vascular-lesions of the council on arteriosclerosis, American-Heart-Association," *Circulation* **92**(5), 1355–1374 (1995).
45. C. T. Binder, "Atherosclerotic plaque," Carotid Ultrasound Webbook & Wiki (2021), <https://www.123sonography.com/atherosclerotic-plaque>.
46. L. H. Timmins, Q. Wu, A. T. Yeh, J. E. Moore Jr., and S. E. Greenwald, "Structural inhomogeneity and fiber orientation in the inner arterial media," *Am. J. Physiol. Heart. Circ. Physiol.* **298**(5), H1537–H1545 (2010).
47. X. Yu, Y. Wang, and Y. Zhang, "Transmural variation in elastin fiber orientation distribution in the arterial wall," *J. Mech. Behav. Biomed. Mater.* **77**, 745–753 (2018).
48. K. Konig, A. Ehlers, I. Riemann, S. Schenk, R. Buckle, and M. Kaatz, "Clinical two-photon microendoscopy," *Microsc. Res. Tech.* **70**(5), 398–402 (2007).
49. D. M. Huland, D. G. Ouzounov, D. R. Rivera, C. M. Brown, and C. Xu, "Intravital multiphoton endoscopy," *Advances in Intravital Microscopy: From Basic to Clinical Research*, R. Weigert, ed., pp. 305–370, Springer Netherlands (2014).